Supplemental Proceedings: Volume 2: Materials Properties, Characterization, and Modeling
TMS (The Minerals, Metals & Materials Society), 2012

THERMAL-MECHANICAL MODEL CALIBRATION WITH BREAKOUT SHELL MEASUREMENTS IN CONTINUOUS STEEL SLAB CASTING

Junya Iwasaki[1], and Brian G. Thomas[2]

[1]Nippon Steel Corp., Yawata Works, Steelmaking Dept.,
1-1 Tobihatacho Tobata-ku, Kitakyusyu-city 804-8501 JAPAN
[2]University of Illinois, Mechanical Science and Engineering,
1206 West Green St., Urbana, IL 61801

Keywords: continuous casting, heat transfer, finite-element, longitudinal cracks, measurements

Abstract

Heat-flow and thermal-stress models of continuous steel slab casting are calibrated with detailed measurements of a breakout and applied to predict longitudinal off-corner crack formation. First, a fluid mass balance is applied together with the measured slide-gate position, mold level, casting speed histories to reconstruct the transient events that occurred during the breakout, including the flow-rate and solidification time histories. An efficient one-dimensional (1-D) heat transfer model of the mold, CON1D, is calibrated to match the measured mold heat flux and thermocouple temperatures, with the help of a full 3-D finite-element model. Using these results, a finite-element thermal-stress model of the solidifying shell was able to match the measured shell thickness profiles, and was applied to reveal insights into interfacial gap conditions and other effects on the formation of off-corner longitudinal cracks and breakouts.

Introduction

Computational models of heat transfer and thermo-mechanical behavior are useful tools to understand quality problems such as longitudinal cracks in continuous casting of steel. Making accurate, quantitative predictions is difficult, however, because many of the phenomena, such as interfacial heat transfer and crack formation, depend on empirical parameters. One way to meet this challenge is to calibrate the models with measurements on the commercial process.

A breakout is the ultimate casting defect. This work performs comprehensive measurements of a breakout at Nippon Steel Yawata Works No.2 strand caster, and presents the casting conditions and data as a benchmark for understanding breakout events, and for model calibration. Finally, the breakout is treated as a longitudinal crack, where the conditions that caused it can be estimated with sufficient accuracy to use as a basis for evaluating hot-tear crack criteria.

Breakout Analysis

The breakout occurred while casting a 252 x 1360 mm slab of plain carbon steel (0.162%C, 0.71%Mn, 0.016%P, 0.006%S, 0.02%Si, 0.039%Al), under generally steady conditions, given in Table 1, 104 minutes after changing heats. Liquidus and solidus temperatures are 1515.4 and 1479.8 ºC. The mold was 258mm thick (top) x 900mm long with 9.5mm taper/side. The mold powder had CaO/SiO_2 ratio of 1.2, with a flux solidification temperature of ~1160 ºC, and viscosity of 0.6P at 1300ºC. The oscillation marks averaged 0.37mm in depth and 3.55mm in width.

Figure 1 contains a schematic of the process and Figure 2 shows pictures of the breakout shell and hole, which was 34,000 mm^2 in area. The breakout occurred on the fixed (inside-radius) wideface (WF), 30mm from the north side (NF) corner, and 1200mm below the top of the shell. Figures 3 and 4 plot several important variables with time before and during the breakout. These data were recorded every one second. Casting speed is constant at 1.4 m/min for over 1000 seconds prior to the breakout. Time of 0 sec is defined when the sliding-gate nozzle was closed completely. Considering the rapid level drop and gradual increase in nozzle opening at –22 sec, the breakout is believed to have started at this time. The meniscus level signal became erroneous at times above –5 sec. Heat flux was constant until ~10s, but variations were observed between the four faces.

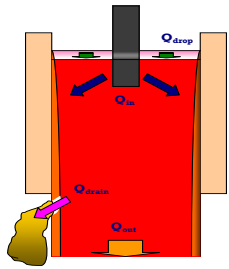

Figure 1. Process schematic and mass flows

Table 1. Casting conditions

Casting speed		23.4 mm/s
SEN submergence depth		230 mm
Pour temperature		1540 ºC
Meniscus dist. from mold top		96mm
Mold conductivity	(WF)	242 W/mK
	(NF)	355 W/mK
Mold heat flux (average)	(fixed WF)	1.279 MW/m^2
	(south NF)	1.294 MW/m^2
	(loose WF)	1.195 MW/m^2
	(north NF)	1.336 MW/m^2

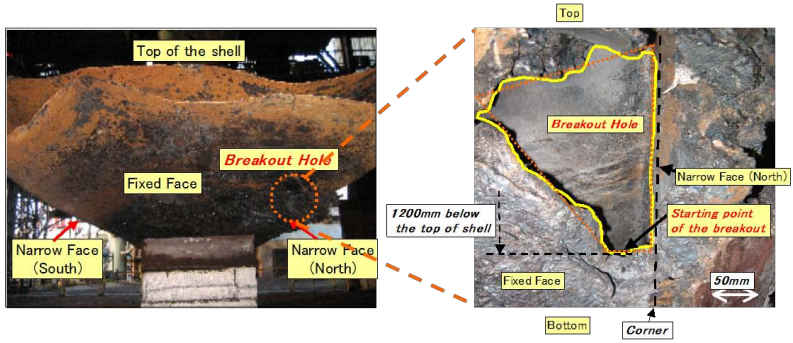

Figure 2. Breakout shell showing view looking down (left) and closeup of hole (right)

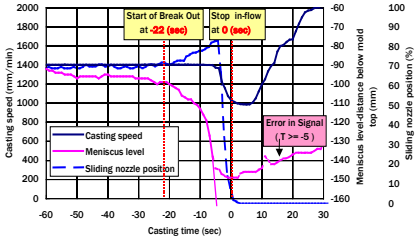

Figure 3. Recorded casting condition histories

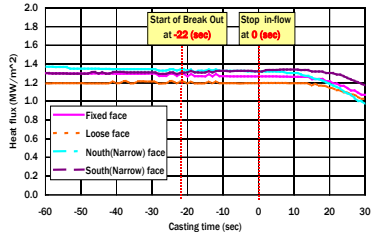

Figure 4. Recorded mold heat flux histories

Estimating flow rates

In order to analyze solidification of each point along the breakout shell, the rate of level drop must be determined during the breakout.[2]? Considering an Eulerian reference frame relative to the steady meniscus position, the following mass balance equation relates the flow rates,

$$Q_{in} + Q_{drop} = Q_{out} + Q_{drain} \tag{1}$$

where Q_{in} is input from sliding nozzle gate, Q_{drop} is flow rate due to the level drop, Q_{out} is output by the moving solid shell, and Q_{drain} is drainage from the breakout hole. Before –22sec, Q_{drain} = 0, and after 0sec, Q_{in} = 0. Figure 1 shows a schematic of these flow rates. The input flow rate, Q_{in}, is found from the time-dependent position of the slide-gate nozzle, X_t, according to a relation found from previous nozzle measurements, given in Figure 5 [1]. The outlet flow rate, Q_{out}, is found from the time-dependent casting speed, slab width, and thickness, as follows:

$$Q_{out} = \rho \times W \times Y \times V_C(t) \tag{2}$$

where ρ is steel density, W is slab width, Y is slab thickness, and V_C is casting speed. Dividing the casting time into two regions, prior to -5s, the liquid level is measured, so Q_{drop} is found by rearranging Eqs. 1-2 as follows:

$$Q_{drop} = \rho \times W \times Y \times \frac{(z_t - z_{t-1})}{(t-(t-1))} \tag{3}$$

Then, Q_{drain} is found from Eq. (1), and the breakout hole size, S_t (mm^2), is found as follows:

$$S_t = \frac{Q_{drain}}{\rho \times v_t}; \qquad \text{where } v_t = \sqrt{2gh_{t-1}}; \qquad \text{where } h_{t-1} = z_{hole-t-1} - z_{t-1} \tag{4}$$

where z_t and z_{t-1} are distance below the steady state meniscus to the liquid level at times t and t-1, v_t is the average speed of fluid draining from the breakout hole at time t, g is gravitational acceleration, h_{t-1} is distance from the liquid level to the breakout hole at time t-1, and $z_{hole-t-1}$ is distance below the steady state meniscus to the breakout hole at time t-1. Figure 6 plots the breakout hole size, including calculations using this method before -5 sec.

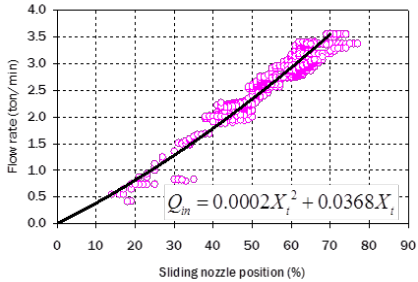

Figure 5. Previous measured relation between flow rate (Q_{in}) and sliding gate position (X_t)

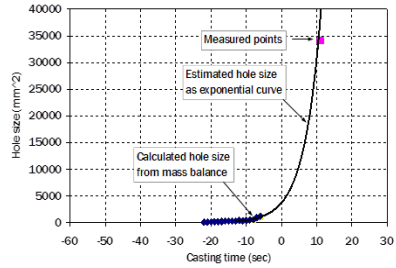

Figure 6. Calculated evolution of the breakout hole size

At times after -5sec, the breakout hole size was estimated with an exponential curve fit:

$$S_t = 3713.7e^{0.2119t} \qquad (5)$$

Finally, the square point in Figure 6 is the measured size of the final breakout hole. From the breakout hole size in Figure 6, Q_{drop} and Q_{drain} were calculated after -5 sec using Eqs. (1), (4) and (5). All four flow rates are plotted in Figure 7. At –4sec, the flow rate due to level drop, Q_{drop} became larger than the outflow from the shell withdrawal at the casting speed, Q_{out}. This means that top of the breakout shell was cast and exposed at this time, as the liquid level dropped below this point. Drainage from the breakout hole Q_{drain} stopped at 11sec.

Estimating solidification time

Figure 8 illustrates the movement of the shell, the liquid level, and the breakout hole during the breakout, relative to the steady-state meniscus level (y=0). The solid lines plot distance versus time histories for several points on the final strand surface, which became the breakout shell. These curves were derived from the time- dependent casting speed data. The bottom of the breakout hole was cast at –59sec. The dotted line indicates liquid level. The results in this figure show that the breakout initiated just below mold exit, and enlarged as it moved downward.

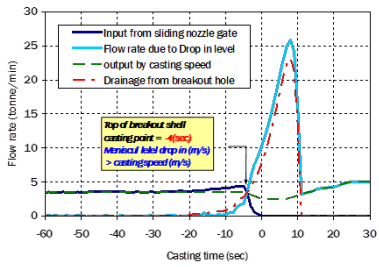

Figure 7. Calculated flow-rate histories

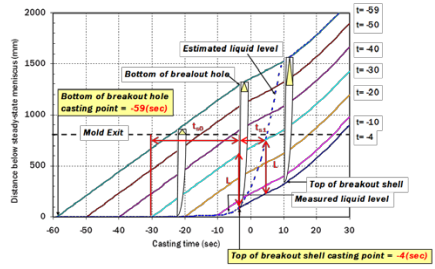

Figure 8. Distance traveled by different points on breakout shell showing distance relationships

Figure 8 can be used to find the total solidification times of each point on the breakout shell, t_s,

$$t_s = t_{s0} + t_{s1}; \qquad \text{where } \int_{t_{s0}}^{t_{-4}} V_C dt = L; \qquad \text{and } \int_{t_{-4}}^{t_{s1}} (\frac{dz}{dt} - V_C) dt = L \qquad (6)$$

where t_{s0} is solidification time for casting at steady-state, (which occurs before -4s) and t_{s1} is the extra solidification time that occurred after the liquid level had dropped below the top of the shell (which occurs after -4sec). An example of these two solidification times is illustrated graphically in Figure 8 for a typical point on the breakout shell (L=540mm below the top) that started solidification at t=-30s. During steady casting, t_{s1}=0.

Solidification times are calculated for every point along the breakout shell and plotted in Figure 9. Relative to steady casting, the breakout shell has more solidification time, especially near the top of the shell, where the extra time is a larger fraction of the total. The measured breakout shell thickness profiles along the fixed wideface (WF) and north narrow face are shown in Figure 10. As expected, the breakout shell is thicker than at steady-state, especially near the top.

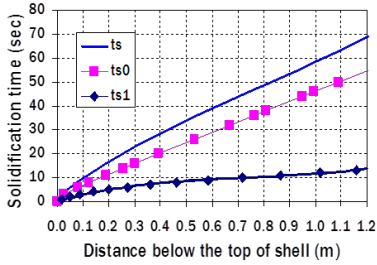

Figure 9. Solidification times during steady casting (t_{s0}) and during the breakout (t_s)

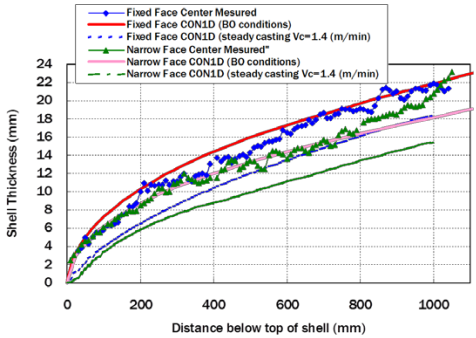

Figure 10. Measured thickness of breakout shell compared with model predictions during the breakout and at steady casting.

The etched solidification structure around the strand perimeter is shown in Figure 11, revealing shell thickness variations around the perimeter of the strand. The shell is thinner at the off-corner region that was cast 5m below where the breakout eventually formed (line B) relative to elsewhere (line A). Specifically, the thickness at B (6.3mm) is 72% of that at A (8.8mm). The narrowface is thicker, corresponding to the higher heat flux on the north NF.

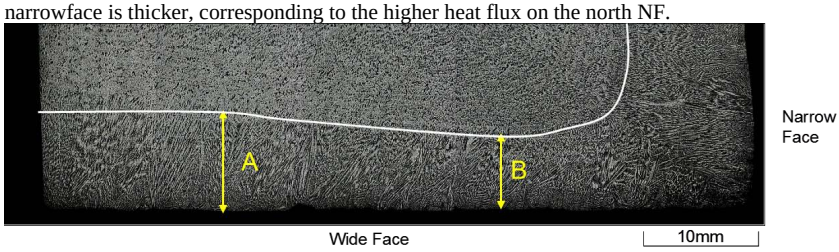

Figure 11 Microstructure of solidified slab cast just before the breakout, showing shell thinning

Mold Temperatures

Temperature measurements were collected from thermocouples embedded in the copper mold walls. The geometry of the wide-face copper mold plate is pictured in Figure 12 in a symmetric-repeating section, including the thermocouple hole. Figure 13 shows the 3-D temperature distribution in this mold predicted with ABAQUS [1,2,3].

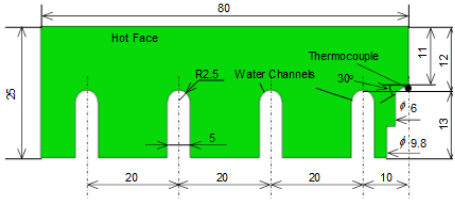

Figure 12. Wideface mold-copper geometry

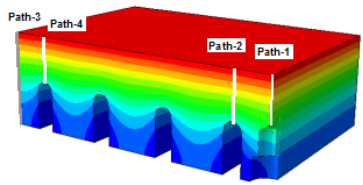

Figure 13. Thermocouple measurements compared with 3-D model predictions

These computations were used to determine "offset distances" to enable CON1D to achieve equal accuracy with 1-D mold temperature predictions [4,5]. Then, CON1D was applied to predict mold heat transfer for the conditions of the breakout. Interfacial parameters were adjusted to achieve a reasonable match with the thermocouple measurements, shell thickness down the mold center, and average mold heat flux. These parameters include gap-layer flux conductivity (1.0 W/mK), the ratio of average solid flux velocity to casting speed (0.085), solid fraction for shell thickness (0.35), and cold face scale thickness (0.002mm). Selected time-averaged thermocouple measurements are shown in Figures 14 and 15, compared with corresponding CON1D predictions at the depth of the thermocouples beneath the mold hotface.

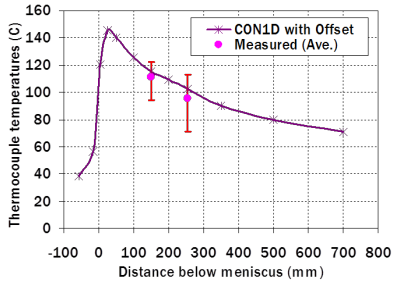

Figure 14. Temperature profile down fixed WF mold at thermocouple location

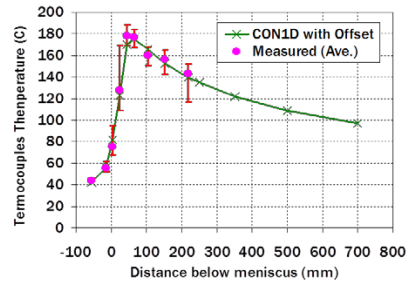

Figure 15. Temperature profile down south NF mold wall at thermocouple location

Mold heat flux

The heat flux profiles found from the calibrated CON1D model are presented in Figure 16. The average of these profiles matches the measurements in Table 1 for the south NF and fixed WF. Further details on the CON1D model and its calibration are presented elsewhere [5-7].

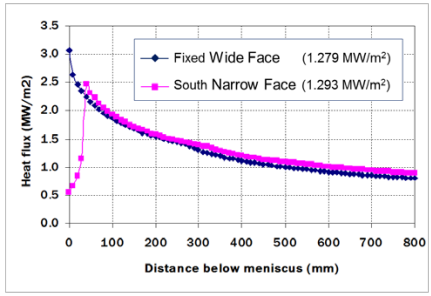

Figure 16. Heat flux profiles predicted down mold

Thermal-mechanical Model and Hot Tearing Criteria

The solidification process was simulated using a computational thermal-mechanical model of a 2-D slice through one quarter of the strand in the mold, using previously-reported models [8-10] in ABAQUS [2]. Using the temperature results from CON1D, constitutive equations for austenite and ferrite presented in previous work [8,10], and a state of generalized plane strain, the displacement, strain, and stress histories of each point within the shell was simulated.

As found in many previous works [8], gaps are computed to form near the corner owing to shrinkage of the shell away from the mold wall. The size of this corner gap was coupled with the heat-flow computation to determine the heat flux as a function of distance around the strand perimeter. Seven different cases were modeled, as summarized in Table II. Most cases assumed the same mold flux thickness profiles computed at the mold center, with the additional gap being filled with air. Case 2 assumed the entire gap to filled with mold flux, and Case 3 assumed the extreme case of the off-corner region being filled with air, to simulate a flux infiltration problem.

The effect of mold distortion was included in Cases 4 and 5, based on three-dimensional ABAQUS simulations of the complete mold plates and water boxes [1,3]. Case 6 included a semi-elliptical-shaped depression (3mm wide x 1mm deep) centered at the critical location, 20-mm from the strand corner. Finally, Case 7 included a trilinear taper of the narrow face, which provided additional squeezing of the wideface all down the mold.

Table II Thermal-mechanical model study

Case	Off-corner Gap Material	Other Effects
1	Flux & air	Ignored
2	Flux only	Ignored
3	Air only	Ignored
4	Flux & air	With mold distortion
5	Flux & air	With 3.8X more mold distortion
6	Flux & air	With depression
7	Flux & air	With trilinear taper

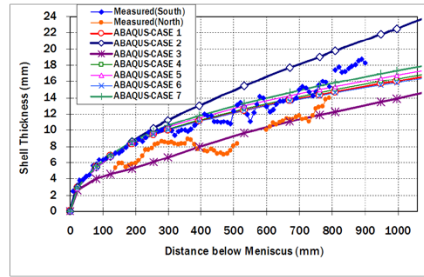

Figure 17. Shell thickness at breakout location

The predicted shell growth along the breakout location near the strand corner is given in Figure 17 for all cases. Most cases are similar, and roughly match the shell thickness measured along the opposite (south) side of the strand. Case 2 is thickest, showing a thicker shell, owing to the improved gap conductivity. Case 3 is the thinnest, owing to the low gap conductivity.

Cracking is predicted by contours of the Zero Ductility Temperature (ZDT), and a hot-tearing damage index from Nagata [11]. Predictions for the seven cases are compared in Figures 18-19.

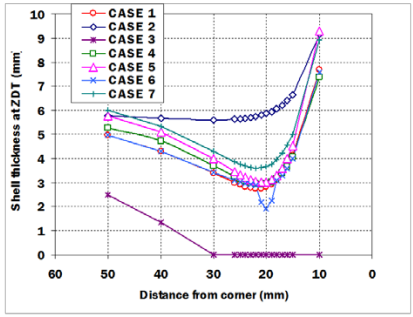

Figure 18. Effective shell thickness based on ZDT at the breakout comparing 7 cases.

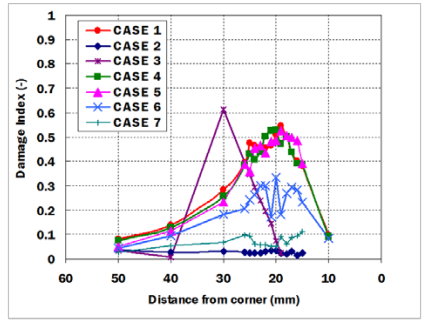

Figure 19. Damage index comparison for 7 cases

As expected, Case 2 had no drop in ZDT near the corner and almost no damage, showing that if liquid mold flux is able to fill the interfacial gap, then longitudinal cracks and breakouts should be avoided. Case 3 had the most severe damage, with ZDT extending to the strand surface and a peak damage index of 0.6 at the eventual breakout location. Surprisingly, Case 6 with the depression had a smaller damage index, owing to the increased temperature of the region causing expansion of the surface that decreased the tension inside the solidifying shell. Case 7 with the trilinear taper had lower damage index as well, owing to compression from the narrowface taper matching better with the natural shrinkage of the shell. None of the cases predicted a damage index exceeding 1, indicating that cracks should not have formed in the mold. Perhaps some other effect, or combination of effects, occurred to cause the breakout, such as tensile stress below the mold, or perhaps the damage criterion needs further work.

Conclusions

This work presents a comprehensive analysis of the formation of a breakout shell on a commercial slab caster, including a simple methodology to extract the detailed evolution of the breakout hole size, flow rates and solidification times during the breakout, based on the measurements. This methodology can serve to augment future analysis of breakout shells.

Further insights are provided by a calibrated heat transfer model, CON1D, which was able to match the measured mold temperatures, shell thickness profiles, average mold heat fluxes, and mold wall temperatures. This case study can serve as a benchmark for further model validation.

A thermal-mechanical model was applied to simulate the breakout, focusing on solidification in the corner. The simulation predicts the most severe damage at the location in the off-corner region of the wideface, where the breakout formed. Many new insights are provided. Achieving good lubrication (with liquid mold flux filling the gap) and optimized narrow face taper should help to avoid longitudinal cracks, and corresponding breakouts. Because the maximum damage index never exceeded 1, further work is needed to quantify longitudinal cracks and breakouts in continuous casting.

References

1) Nippon Steel Corp., Yawata Works, private communication, 2008.
2) ABAQUS 6.9-1, 2009, Dassault Simulia, Inc., 166 Valley Street, Providence, RI, USA.
3) Hibbeler, L.C., and B.G. Thomas, "Thermal Distortion of Funnel Molds", AISTech 2011, Indianapolis, IN, May 2-5, 2011, Assoc. Iron Steel Technology, Warrendale, PA, 2011.
4) Langeneckert, M., MS Thesis, University of Illinois, 2001.
5) Santillana, B., L.C. Hibbeler, et al., ISIJ International 48(10), 2010, pp. 1380-1388.
6) Meng, Y. and B.G. Thomas, Metal. & Material Trans. 34B(5), 2003, pp. 685-705.
7) Meng, Y., B.G. Thomas, et al., Canadian Metallurgical Quarterly 45(1), 2006, pp. 79-94.
8) Li, C. and B. G. Thomas, Metal. & Material Trans. B. 35B(6), 2004, pp. 1151-1172.
9) Hibbeler, L.C., B. Santillana, et al., Metallurgia Italiana 6(2), 2009, pp. 1-10.
10) Koric, S. and B.G. Thomas, 66(12), 2006, pp. 1955-1989.
11) Nagata et al., Tetsu- to- Hagane, 76;2, 1990, p. 214

Acknowledgements

The authors wish to thank Nippon Steel for support of this work and providing data. This work was supported by the Continuous Casting Consortium at the University of Illinois and the National Center for Supercomputing Applications is thanked for advanced computing resources.